

Branching ratio measurement of a "Lambda" system in Tm^{3+} : YAG under magnetic field

A. Louchet, J. S. Habib, V. Crozatier, I. Lorgeré, F. Goldfarb, F. Bretenaker, J.-L. Le Gouët
*Laboratoire Aimé Cotton, CNRS-UPR 3321, Bâtiment 505,
Campus Universitaire, 91405 Orsay Cedex, France*

O. Guillot-Noël, Ph. Goldner
*Laboratoire de Chimie de la Matière Condensée de Paris, CNRS-UMR 7574, ENSCP,
11 rue Pierre et Marie Curie, 75231 Paris Cedex 05, France*

(Dated: July 5, 2021)

A three-level Λ system in Tm^{3+} doped YAG crystal is experimentally investigated in the prospect of quantum information processing. Zeeman effect is used to lift the nuclear spin degeneracy of this ion. In a previous paper [de Seze *et al.* Phys. Rev. B, **73**, 85112 (2006)] we measured the gyromagnetic tensor components and concluded that adequate magnetic field orientation could optimize the optical connection of both ground state sublevels to each one of the excited state sublevels, thus generating Λ systems. Here we report on the direct measurement of the transition probability ratio along the two legs of the Lambda. Measurement techniques combine frequency selective optical pumping with optical nutation or photon echo processes.

PACS numbers: 42.50.Gy, 42.50.Md, 71.70.Ej

I. INTRODUCTION

There is an ongoing interest for macroscopic quantum processes, especially in the perspective of quantum memories and several groups are currently working on performing storage and retrieval of a quantum state of light into an atomic system. Most quantum memory processes rely on the storage of a quantum signal into an atomic spin coherence, which is free from spontaneous emission. The optical excitation carrying the information resonantly excites an atomic transition. A control pulse then converts the optical coherence into a hyperfine long-lived coherence. Another control pulse can eventually change the spin coherence back into an optical coherence and allow the retrieval of the stored signal. This quantum memory scheme can be achieved in a three-level Λ system, where two spin states are connected to a common upper level by optical transitions (cf Fig. 1).

The mapping of a quantum state of light over a macroscopic atomic ensemble has been demonstrated in various materials such as atomic vapors¹ or cold atom clouds². The full quantum memory scheme has recently been

achieved in cold atomic clouds of rubidium³. However, rare-earth ion-doped crystals also appear as promising candidates for quantum storage applications. They offer properties similar to atomic vapors with the advantage of no atomic diffusion. At low temperature (< 4 K), the optical coherence lifetime can reach several ms, and a hyperfine coherence lifetime has been extended to tens of seconds in Pr-doped Y_2SiO_5 (YSO)⁴. Given the absence of atomic motion, extremely long population lifetime can be observed. Electromagnetically induced transparency and "slow light"⁵ have been demonstrated in rare-earth ion-doped crystals, along with storage times greater than a second⁶.

Among all the rare-earth ions (lanthanides), non-Kramers ions with an even number of $4f$ electrons exhibit the longest coherence lifetime in the absence of external magnetic field⁷. With the additional condition on the hyperfine splitting to be of the order of a few tens of MHz in the electronic ground state, the rare earth ions are restricted to praseodymium and europium. Both Pr^{3+} and Eu^{3+} ions have been extensively studied over the past 20 years^{8,9,10,11,12,13,14}. However, only dye lasers are available at operation wavelengths in Pr^{3+} and Eu^{3+} doped crystals. For instance, Pr^{3+} : YSO and Eu^{3+} : YSO are respectively operated at 606 nm and 580 nm. Alternatively, other non-Kramers rare-earth ions such as thulium fall within reach of more tractable lasers.

Tm^{3+} : $\text{Y}_3\text{Al}_5\text{O}_{12}$ (YAG) has been widely studied in the field of coherent transient-based signal-processing schemes^{15,16,17,18} and lasers^{19,20}. It is especially attractive because the $^3H_6(0) \rightarrow ^3H_4(0)$ transition at 793 nm is in the range of semi-conductor lasers which can be stabilized to better than 1 kHz²¹.

Although the only isotope of thulium ^{169}Tm ions has a $I = 1/2$ nuclear spin, it does not exhibit hyperfine structure at zero magnetic field because of J quench-

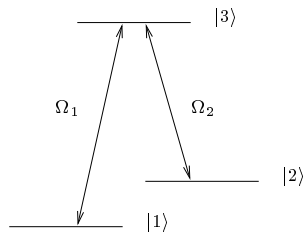


FIG. 1: Three-level Λ system coupled by two lasers. Ω_1 and Ω_2 are the Rabi frequencies that characterize the atom-laser interaction.

ing²². Lifting the nuclear spin degeneracy with an external magnetic field offers a way to build a Λ -system provided the magnetic field induces different spin-state mixing in ground and excited electronic states. In an earlier paper²³ we showed that this was the case for a specific magnetic field orientation with respect to the crystalline axes. We determined the field direction that gives maximum branching ratio between the two optical transition probabilities in the Λ system thus created. In addition, a lower bound to the branching ratio was derived from the experimental measurement of the gyromagnetic factors.

Further characterization of this Λ system includes direct experimental measurement of the optimal branching ratio. This is the purpose of this study. The paper is arranged as follows. In Sec. II we summarize the previous results concerning the building of a Λ system in Tm^{3+} :YAG. In Sec. III the experimental setup is described. In Sec. IV spectral hole-burning is presented and discussed in the case of Tm^{3+} :YAG, and we measure the population lifetime of the ground sublevels. In Sec. V we show that each transition can be individually excited and we measure their relative strengths by optical nutation and two-pulse photon echoes. From these experiments we derive an experimental value of the branching ratio.

II. BUILDING A Λ SYSTEM IN Tm^{3+} :YAG

This section is a brief reminder of the discussion presented in a previous paper²³.

Let us consider the optical transition at 793 nm connecting the fundamental levels of the Stark multiplets 3H_6 and 3H_4 of Tm^{3+} in YAG. Application of an external magnetic field lifts the nuclear spin degeneracy by splitting the electronic levels. As shown in Fig. 2, a three-level Λ system would involve the two hyperfine sublevels of the ground state ${}^3H_6(0)$ and one hyperfine sublevel of the excited state ${}^3H_4(0)$. If the interaction with the magnetic field is restricted to the Zeeman effect, the electronic levels split into $m_I = 1/2$ and $m_I = -1/2$ spin levels. One of the two optical transitions of the Λ is forbidden. Indeed the selection rule $\Delta m_I = 0$ forbids any electronic excitation to flip the nuclear spin. Fortunately, the coupling effect of the Zeeman electronic and the hyperfine interactions mixes the nuclear spin states and may lead to comparable transition strengths for the two legs of the Λ if the magnetic field is suitably oriented. As a consequence, spin-flipping transitions $|1\rangle \rightarrow |4\rangle$ and $|2\rangle \rightarrow |3\rangle$ are no longer forbidden. The atomic states can be represented as the product of an electronic state and a nuclear spin state. The ground level nuclear spin states are derived from the excited level nuclear spin states by a unitary transformation. Therefore the 4 transition dipole moments satisfy:

$$\begin{cases} \langle 1|\mu|3\rangle = \langle 2|\mu|4\rangle = \mu_s \\ \langle 1|\mu|4\rangle = -\langle 2|\mu|3\rangle = \mu_w \end{cases} \quad (1)$$

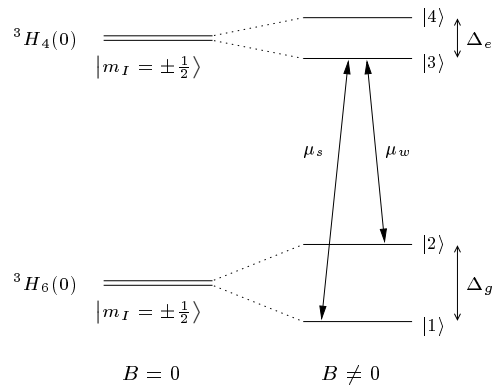


FIG. 2: Building a three-level system with nuclear spin levels in thulium.

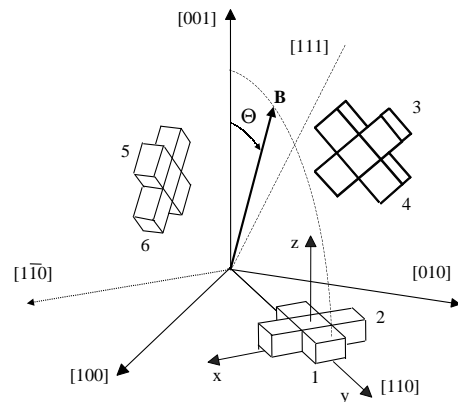


FIG. 3: Tm substitution sites in the YAG matrix. In each site, the transition dipole moment $\vec{\mu}$ is represented by an oblong and is directed along the local Oy axis. Here the local frame x, y, z is given for site 1. The direction of the magnetic field \mathbf{B} is defined by angle Θ .

The weak (respectively, strong) transition dipole moments are referred to as μ_w (respectively, μ_s). The branching ratio R is the ratio of the transition probabilities along the two legs of the Λ :

$$R = \frac{|\langle 2|\mu|3\rangle|^2}{|\langle 1|\mu|3\rangle|^2} = \frac{\mu_w^2}{\mu_s^2} \quad (2)$$

In the YAG crystal, Tm^{3+} ions substitute for yttrium ions in 6 crystallographically equivalent but orientationally inequivalent sites depicted in Fig. 3. Because of the site symmetry (D_2), the optical transition dipole moment is oriented along the Oy local axis of each site. Let the light beam propagate along $[1\bar{1}0]$. Two linear polarization directions are considered.

When it is directed along $[111]$, the optical electric field \mathbf{E} is perpendicular to the electric dipoles $\vec{\mu}$ of sites 2, 4 and 6. The only excited sites are then 1, 3 and 5. They interact with the light beam with the same Rabi frequency $\Omega = \vec{\mu} \cdot \mathbf{E} / \hbar$ and therefore contribute the same amount to the crystal optical density.

Alternatively, when the light beam is polarized along direction $[\bar{1}\bar{1}1]$, the only excited sites are 1, 4 and 6. Their Rabi frequencies are equal.

For a given magnetic field orientation, the field coordinates are specific to each site local frame. Since the gyromagnetic tensor is strongly anisotropic in both electronic levels, the 6 sites exhibit different hyperfine splittings:

$$\Delta_{g,e} = \sqrt{\gamma_{xg,e}^2 B_x^2 + \gamma_{yg,e}^2 B_y^2 + \gamma_{zg,e}^2 B_z^2} \quad (3)$$

where g and e denote the ground and excited electronic states, and where the gyromagnetic tensor γ and the magnetic field \mathbf{B} coordinates are given in the local frame. Let \mathbf{B} be applied in the bisector plane defined by crystalline axes $[001]$ and $[110]$. The magnetic field direction is defined by angle Θ formed with direction $[001]$, as illustrated in Fig. 3. For any magnetic field orientation within the bisector plane, ions in sites 3 and 5 experience the same field. Hence they have identical Zeeman splittings and equal branching ratios. Similarly, ions in sites 4 and 6 experience the same magnetic field and exhibit equal branching ratio.

The branching ratio for ions in sites 3 and 5 was calculated from theoretical gyromagnetic factors for any magnetic field orientation²⁴. When the magnetic field is in the bisector plane, Fig. 4 shows that the theoretically predicted branching ratio goes through a maximum $R_{\max} = 0.24$. Besides, Fig. 4 shows that the accurate orientation of the magnetic field is critical around the maximum branching ratio orientation.

The experimental measurement of the gyromagnetic tensor coefficients²³ made it possible to determine a lower boundary for the maximum branching ratio:

$$R_{\max} \geq 0.13 \pm 0.02 \quad (4)$$

These measurements also yielded the magnetic field orientation that gives maximum branching ratio for ions in sites 3 and 5: $\Theta = -49.4 \pm 0.2^\circ$. This is rather close to direction $[\bar{1}\bar{1}1]$ (corresponding to $\Theta = -\arccos(1/\sqrt{3}) = -54.8^\circ$).

III. EXPERIMENTAL SETUP

The system is excited and probed with an extended cavity semiconductor laser operating at 793 nm. It is stabilized on a high-finesse Fabry-Perot cavity through a Pound-Drever-Hall servo-loop²¹. It is amplified with a Toptica BoosTA laser amplifier. A single-mode fiber spatially filters the beam. At the end of the fiber one measures up to 100 mW output power, depending on the amplifier adjustment.

The 0.1 at.% Tm^{3+} : YAG crystal is 5 mm thick. It is cut perpendicular to direction $[1\bar{1}0]$ along which the laser beam propagates (cf Fig. 3). We use a commercial Oxford 6T Spectromag SM4 cryostat. The adjustable magnetic field is generated by superconducting coils immersed in liquid helium. The sample is cooled down to 1.9 K.

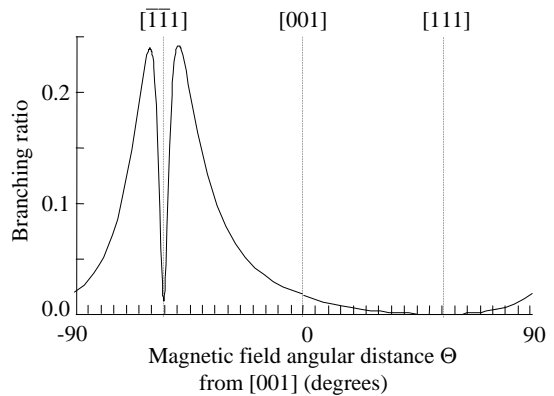


FIG. 4: Theoretical branching ratio variations for ions in sites 3 and 5 as a function of magnetic field orientation²⁴.

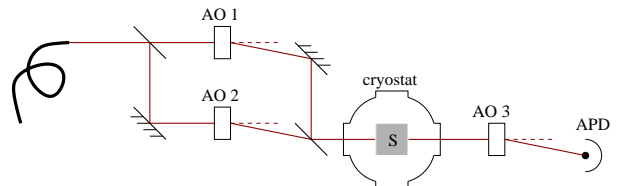


FIG. 5: (color online) Schematic of optical setup after the fiber. AO 1, 2 and 3 are acousto-optic devices, S is the Tm:YAG sample, and APD is the avalanche photodiode.

Fig. 5 shows the optical setup after the fiber. Pulse sequences are shaped by an Arbitrary Waveform Generator (Tektronix AWG 520) that monitors two external acousto-optic shifters (AO 1 and AO 2). The acousto-optic shifters are imaged on the sample (S) so that the beam does not move across the sample when the frequency is varied. The spot size on the crystal is adjusted to $100 \mu\text{m}$, except in the experiments described in Sec. IV B, where the spot size is $800 \mu\text{m}$. The transmitted light is then collected on an avalanche photodiode (APD) HAMAMATSU C5460. An acousto-optic modulator (AO 3) protects the detector from possible strong burning pulses.

IV. HOLE BURNING SPECTROSCOPY

A. Spectral hole burning in an inhomogeneously broadened 4-level system

In thulium, the optical transition at 793 nm exhibits a very large inhomogeneous broadening $\Gamma_{\text{inh}} \simeq 20 \text{ GHz}$. Application of a magnetic field splits each electronic level into a pair of hyperfine sublevels with a Zeeman splitting of the order of 10 to 400 MHz/T, depending on the magnetic field orientation with respect to the local site axes. A field lower than 1 Tesla does not modify the absorption spectrum since the inhomogeneous linewidth is much larger than the Zeeman splitting. Because of inhomoge-

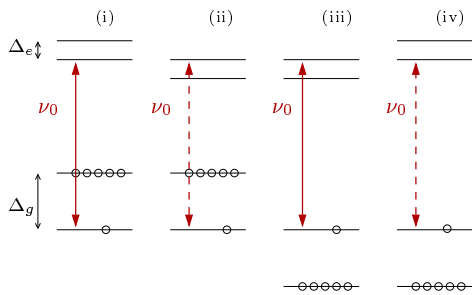


FIG. 6: (color online) Optical pumping of four classes of ions to the non-resonant ground sublevel by excitation at frequency ν_0 . Solid lines: strong transitions. Dashed lines: weak transitions. Ions are depicted by open circles.

neous broadening, a laser excitation at given frequency ν_0 simultaneously excites 4 different classes of ions, as illustrated in Fig. 6. Each class refers to a specific ground and excited state sublevels that are connected by the incoming field. Initially, in each ion class both ground sublevels are equally populated. This is even true at working temperature ($T = 2$ K), since the level splitting is much smaller than $k_B T/h \simeq 30$ GHz.

When the sample is exposed to sustained incident light at ν_0 , it experiences optical pumping that tends to unbalance the ground level state distribution. Ions in the resonantly excited sublevel are transferred to the off-resonant sublevel (cf Fig. 6). This gives rise to a hole in the absorption spectrum at frequency ν_0 . Besides, since we consider 4-level systems, additional features appear. Two side holes are observed at $\nu_0 \pm \Delta_e$, where the probe field excites transitions from the depleted ground sublevel to the other excited state sublevel. Conversely, transitions from an overpopulated ground sublevel to either excited sublevel give rise to antiholes in the absorption spectrum. Such antiholes are observed at $\nu_0 \pm \Delta_g$ and $\nu_0 \pm (\Delta_g \pm \Delta_e)$.

Depending on the sublevels they connect, the various transitions excited by the probe beam can be sorted as weak or strong ones. It should be noted that at least one strong transition contributes to any hole and antihole, except for the antiholes located at $\nu_0 \pm (\Delta_g \pm \Delta_e)$. These antiholes arise from a probing process along a weak transition in the ion classes (ii) and (iv) of Fig. 6. As a result, the observation of an antihole at this position shall bear evidence that the nuclear spin flip selection rule is actually relaxed.

We perform spectral hole-burning in $\text{Tm}^{3+}:\text{YAG}$. A 0.19 T magnetic field is oriented in the direction that is expected to give maximum branching ratio for ions in sites 3 and 5 ($\Theta = -49.4^\circ$, cf Sec. II). The laser beam is linearly polarized in direction [111] so that only sites 1, 3 and 5 are excited. The burning step consists in a series of ten 50 μs pulses every 10 ms. Then the sample is probed with a weak 1 ms long pulse chirped over a 35 MHz interval. The burning and probing sequence is repeated every 150 ms. Transmitted probe intensity is collected on a photodiode, averaged over 8 shots and

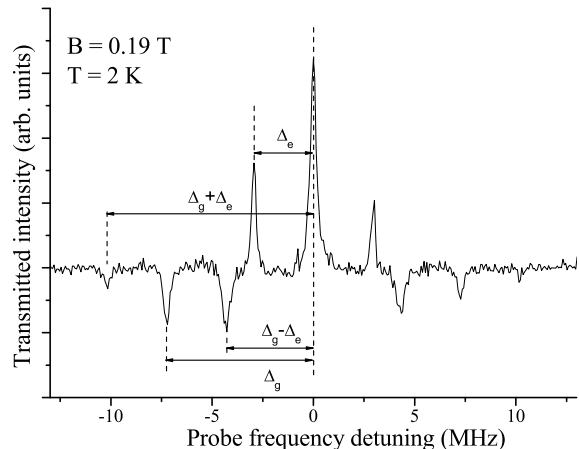


FIG. 7: Hole-burning transmission spectrum for $\text{Tm}^{3+}:\text{YAG}$ under a 0.19 T magnetic field. The spectral holes and antiholes correspond to site 3 and 5 ions. The features corresponding to site 1 are out of the probing spectral window.

plotted in Fig. 7. The holes and antiholes are ascribed to sites 3 and 5. We measured the ground and excited splittings for these two sites in this field direction:

$$\Delta_g/B = 38.2 \pm 1 \text{ MHz/T} \quad (5)$$

$$\Delta_e/B = 15.5 \pm 0.7 \text{ MHz/T} \quad (6)$$

where B is the magnetic field amplitude. This agrees with the calculated splittings derived from the experimental gyromagnetic tensor components²³: $\Delta_g/B = 36.0 \pm 1$ MHz/T and $\Delta_e/B = 16.0 \pm 0.8$ MHz/T. The ground level gyromagnetic tensor values are close to those measured by Schmidt in TmAG by Nuclear Magnetic Resonance²⁵.

One can see in Fig. 7 that the antiholes are generally wider than the holes. This suggests that the inhomogeneous broadening of the Zeeman splitting is larger in the ground state than in the excited state.

The hole-burning features associated with site 1 cannot be seen in Fig. 7 because the Zeeman splitting for site 1 is over 60 MHz/T for this magnetic field orientation.

B. Sublevel population lifetime

The hole-burning spectrum is erased by return to thermal equilibrium. To measure the corresponding decay rate, we measure the central hole depth as a function of delay between pumping and probing steps. The sample is cooled down to $T = 1.9$ K. A 0.45 T magnetic field is applied in direction $\Theta = -54.5^\circ$, very close to $[\bar{1}\bar{1}1]$. It should be noted that this is not the optimal direction discussed in Sec. II.

The light beam is polarized in direction $[\bar{1}\bar{1}1]$ so that only sites 1, 4 and 6 are excited, with identical Rabi fre-

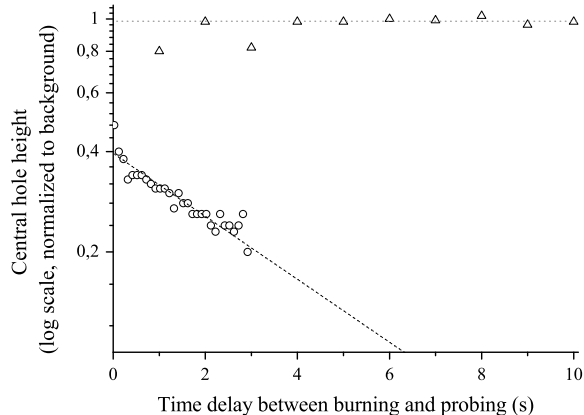


FIG. 8: Decay of central spectral hole after burning operation for sites 1, 4 and 6 (triangles) and sites 3 and 5 (circles). For these two measurements an exponential function is fitted (dashed lines). In this experiment only, the 0.45 T magnetic field is along $[\bar{1}\bar{1}1]$.

quency. In addition, since they are magnetically equivalent, their Zeeman splittings are equal ($\Delta_g = 181.4$ MHz and $\Delta_e = 36.9$ MHz) and they exhibit the same population lifetime. Fig. 8 shows that the central hole does not decay for 10 seconds following excitation. In other words, the population lifetime relative to sites 1, 4 and 6 for this magnetic field orientation and strength is estimated to a few minutes.

The light beam is then polarized along $[111]$ so as to excite sites 1, 3 and 5 with identical Rabi frequency. Since we are interested in measuring the sublevel population lifetime for sites 3 and 5 only, we isolate ions in sites 3 and 5 by means of a bleaching process: a strong beam chirped over a 25 MHz interval optically pumps a large spectrum range of ions in site 1 to the non-resonant very long lifetime ground sublevel. Site 3 and 5 ions also undergo optical pumping but the chirp amplitude is much larger than the ground sublevel splitting $\Delta_g = 6.9$ MHz. As a consequence, a large fraction of ions in sites 3 and 5 is pumped back to the initial sublevel. Three seconds after this bleaching process, we perform ordinary spectral hole-burning and observe the decay of the central hole depth by varying the delay between burning and probing (cf Fig. 8). An exponential fit gives a population lifetime of 4.5 ± 0.5 s for sites 3 and 5.

Therefore in crystallographically equivalent sites 1,3 and 5, the sublevel population lifetime apparently increases with the ground state splitting. At present we cannot explain this behavior. In contradiction with our measurements, N. Ohlsson *et al.* observed longer lifetimes for smaller splittings in a given site²⁶.

Since the spin level thermalization does not involve optical transitions, we expect the corresponding decay rate to be insensitive to a small angle rotation of the magnetic field. Indeed, when \mathbf{B} orientation is varied from

	$\Theta = -54.5^\circ$	$\Theta = -49.4^\circ$ (maximum R)
site 1	328 MHz/T	306 MHz/T
sites 3, 5	15 MHz/T	36 MHz/T

TABLE I: Calculated values for normalized ground splitting Δ_g/B in different sites, for two specific field orientations.

$\Theta = -54.5^\circ$ to $\Theta = -49.4^\circ$, the branching ratio of the optical transitions strongly increases (cf Fig. 4), but the level splitting Δ_g varies little, as shown in Table I. The decay rate is expected to be mainly sensitive to this level splitting.

Before sites 3 and 5 can be coherently manipulated for quantum storage, it is necessary to prepare site 1 ions so that they do not interfere. Their very long population lifetime guarantees that a bleaching process can store them for a long time in a non-resonant ground sublevel. As for sites 3 and 5, a spin level lifetime of a few seconds is long enough for coherent manipulation.

V. BRANCHING RATIO MEASUREMENT

In order to precisely compare the optical transitions along the two legs of the Λ , we resort to coherent processes along with frequency selective optical pumping. This enables us to isolate the weak optical transition contribution.

A. Optical nutation

A two-level system driven by a resonant monochromatic field \mathbf{E} oscillates between its ground and excited states at Rabi frequency $\Omega = \vec{\mu} \cdot \mathbf{E}/\hbar$. Along with this population oscillation, the system emits an induced radiation that modulates the driving field at frequency Ω . This gives a direct and robust way to measure the Rabi frequency of a transition even when the inhomogeneous broadening is infinite and the beam spatial profile is not uniform: for an infinitely inhomogeneously broadened medium driven by a stepfunction gaussian laser beam at $t = 0$, the transmitted signal takes the form of damped oscillations²⁷:

$$\frac{I_{\text{nut}}(t)}{I_0} = 1 - 2(1 - 10^{-D}) \frac{J_1(\Omega t)}{\Omega t} \quad \text{for } t > 0 \quad (7)$$

where I_0 is the incoming beam intensity, D is the optical density of the sample, Ω is the Rabi frequency of the ion-laser interaction in the center of the beam and J_1 is the Bessel function of order 1. This expression is valid if the optical density of the sample is small ($D < 0.5$). According to Eq. 7, the first maximum of $I_{\text{nut}}(t)$ is located at $t_{\text{max}} = 5.1/\Omega$, therefore the Rabi frequency can be directly obtained from the nutation signal.

The optical density D can be assessed by comparing the transmission of the material at $t = 0$ with its trans-

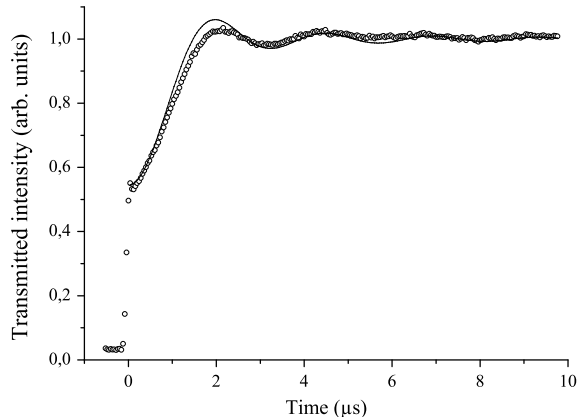


FIG. 9: Optical nutation signal with zero magnetic field (open circles) when a step-function monochromatic excitation is applied at $t = 0$. The signal is fitted according to Eq. 7 with $\Omega = 2.6$ MHz and $D = 0.32$ (solid line).

mission after a long exposure to laser light:

$$D = \log_{10} \frac{I_{\text{nut}}(t \rightarrow \infty)}{I_{\text{nut}}(t = 0)} \quad (8)$$

This way, one can measure the optical density of the material with a single nutation temporal profile. Besides, the optical density is proportional to μ^2 and to the number of active atoms. If optical nutation is performed on each transition, then the optical density measurement gives direct access to the relative dipole moments of the weak and strong transitions.

We first observe optical nutation on the two-level system formed by Tm^{3+} : YAG at zero magnetic field. The transmitted signal is displayed in Fig. 9. The sample is cooled down to $T = 3$ K and is excited with a $10 \mu\text{s}$ resonant light pulse polarized along [111]. For this light polarization, sites 1, 3 and 5 participate in absorption with equal Rabi frequency and each one of them contributes one third to the total optical density $D_0 = 0.32$.

Let us apply a magnetic field in the direction that is expected to give maximum branching ratio for sites 3 and 5 (cf Sec. II). Application of a magnetic field splits the electronic levels, the ions being equally distributed in both ground sublevels. As mentioned in Sec. IV A, this does not change the absorption profile of the sample, so the nutation signal is not modified.

We now apply $10 \mu\text{s}$ pulses. The sample temperature is decreased gradually from 5 K to 2 K. As long as thermalization processes dominate, the system returns to thermal equilibrium between successive pulses. As the temperature goes down, thermalization gets slower. Ultimately, resonant sublevel depletion by optical pumping supersedes repopulation by relaxation processes (see Fig. 6) and the nutation signal disappears.

The repopulation process can be assisted by optical repumping. If one tunes the repumping laser to

$\nu_R = \nu_0 - \Delta_g$ so as to counterbalance optical pumping at ν_0 , only ions in sites 3 and 5 from classes (i) and (ii) are pumped back into the initial ground sublevel [see Fig. 10(a)]. All ions in site 1, as well as ions in sites 3 and 5 with excitation schemes (iii) and (iv), stay off resonance with the repumping beam. In a given class of ions, the steady-state fraction of ions in the resonant sublevel reads as

$$\rho = \frac{r + \kappa}{p + r + 2\kappa} \quad (9)$$

where p , r and κ respectively stand for the pumping rate, the repumping rate and the temperature dependent relaxation rate. In the absence of optical excitation this fraction reduces to $\rho = 1/2$, which means that the ground state population is evenly shared between the two sublevels. When $r = 0$ and $p \gg \kappa$, all ions are pumped to the off-resonance sublevel and $\rho = 0$. When $r, p \gg \kappa$ the relative population reduces to $\rho = r/(p + r)$.

Optical pumping consists in repeated excitation and relaxation processes. Excitation is carried out by a series of $10 \mu\text{s}$ pulses. Within this $10 \mu\text{s}$ pulse duration the transition at ν_0 is bleached, resulting in evenly populated ground and upper levels. As will be shown later in this section, this is true even when the excitation takes place along the weak transition. Therefore the excitation process brings the system in the same final state, whatever excitation path is followed.

Relaxation to the ground state strongly differs from spontaneous emission decay. Indeed, non-radiative processes dominate, proceeding through the intermediate states 3H_5 and 3F_4 . We assume here that these stepwise relaxation processes relax the nuclear spin selection rule. To sum up, neither excitation nor relaxation depends on the transition strengths, and the same value of ρ is used for classes (i) and (ii).

The electronic transition dipole moment does not depart from its zero magnetic field value. Since only 2 sites out of 3 participate in the absorption, the optical density at stake here reads as

$$D_{s+w} = \frac{2}{3} D_0 \left(\frac{\mu_s^2}{\mu_s^2 + \mu_w^2} \rho + \frac{\mu_w^2}{\mu_s^2 + \mu_w^2} \rho \right) = \frac{2}{3} D_0 \rho \quad (10)$$

where D_0 is the optical density at zero magnetic field.

Similarly, if the repumping laser is tuned to $\nu_R = \nu_0 + \Delta_g + \Delta_e$ [cf Fig. 10(b)], only ions from system (iv) are repumped to the resonant sublevel: the nutation signal is ascribed to ions in sites 3 and 5 resonating on a weak transition. The optical density is expected to be much smaller than D_0 and reads as

$$D_w = \frac{2}{3} D_0 \frac{\mu_w^2}{\mu_s^2 + \mu_w^2} \rho = \frac{2}{3} D_0 \frac{R}{1 + R} \rho \quad (11)$$

Finally, if $\nu_R = \nu_0 + \Delta_g - \Delta_e$, only ions from system (iii) are repumped to the resonant sublevel: the nutation signal is ascribed to ions in sites 3 and 5 resonating on a

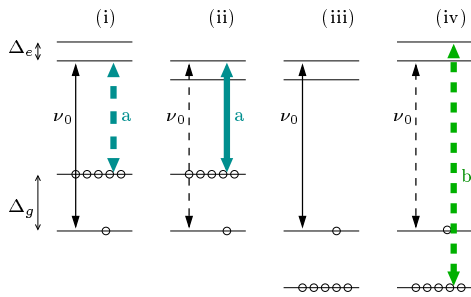


FIG. 10: (color online) Examples of repumping schemes. Four classes of ions are excited at frequency ν_0 . The repumping frequencies are displayed as thick solid (respectively, dashed) arrows along strong (respectively, weak) transitions. (a) $\nu_R = \nu_0 - \Delta_g$: only systems (i) and (ii) participate in the nutation signal, along a strong transition for system (i) and along a weak transition for system (ii). (b) $\nu_R = \nu_0 + \Delta_g + \Delta_e$: only ions in system (iv) participate in the nutation signal, along a weak transition.

strong transition. The optical density reads as

$$D_s = \frac{2}{3} D_0 \frac{\mu_s^2}{\mu_s^2 + \mu_w^2} \rho = \frac{2}{3} D_0 \frac{1}{1+R} \rho \quad (12)$$

The combination of optical pumping and repumping processes makes it possible to isolate a nutation signal related either to a weak or to a strong transition. The transmitted intensity for various repumping frequency values is displayed in Fig. 11. The repetition rate is 50 s^{-1} , the sample temperature is $T = 2 \text{ K}$ and the incident intensity is the same whatever the repumping frequency value.

The optical density of the sample under zero magnetic field is $D_0 = 0.36$ according to Eq. 8 applied to Fig. 11(a). When a 0.3 T magnetic field is applied, the sample becomes transparent: the damped oscillations disappear and the transmitted intensity is almost constant [cf Fig. 11(d)].

The repumping process consists in a series of ten $100 \mu\text{s}$ chirps over 1 MHz around the repumping frequency ν_R . It is applied between successive excitation pulses. In Fig. 11(b) we plotted the transmitted intensity when a repumping beam is applied at frequency $\nu_0 - \Delta_g$. The optical density is measured on the nutation signal: $D_{s+w} = 0.167$. Eq. 10 gives the relative population of the resonant sublevel in systems (i) and (ii): $\rho = 69\%$. Besides, in both cases (a) and (b) of Fig. 11, the nutation signal is associated with exciting strong transitions as well as weak transitions. This is why the Rabi frequency and hence the position of the first maximum in the nutation signal do not change.

Finally, in Fig. 11(c) we plotted the transmitted intensity for a repumping beam at $\nu_0 + \Delta_g + \Delta_e$. The optical density of the sample excited only along a weak transition is very small: $D_w = 0.018 \pm 0.004$. No damped oscillations are visible, but the transmitted intensity slowly increases with time during excitation. The experimental

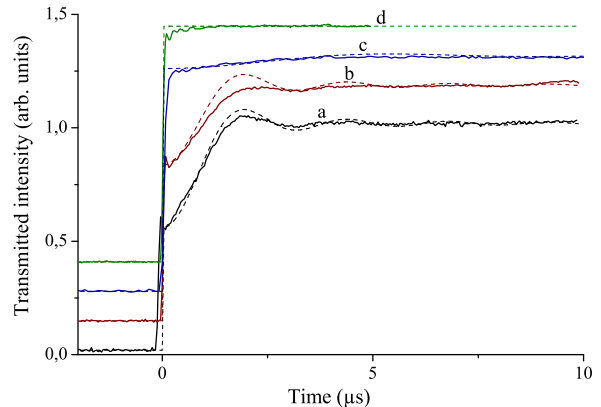


FIG. 11: (color online) Optical nutation signals for various repumping frequencies. The four solid traces are obtained with the same incoming laser intensity. a: with zero magnetic field, b: with magnetic field and repumping at frequency $\nu_R = \nu_0 - \Delta_g$, c: with magnetic field and repumping at frequency $\nu_R = \nu_0 - \Delta_g - \Delta_e$, d: with magnetic field but no repumping beam. The dashed traces are theoretical curves given by Eq. 7 and fitted to the experimental data. The graphs are vertically offset for clarity.

data clearly show that the position of the first maximum in nutation signal (c) is different from cases (a) and (b), even though it cannot be accurately located. This proves that signal (c) does not come from a residual signal emitted along a strong transition.

According to Eqs. 10 and 11, the ratio of D_w and D_{s+w} finally leads to:

$$R = \frac{\mu_w^2}{\mu_s^2} = 0.12 \pm 0.03. \quad (13)$$

which is consistent with the lower boundary given in Eq. 4 derived from gyromagnetic tensor measurements²³.

The position of the first maximum of nutation profile for the weak transition is \sqrt{R} times the corresponding position for the strong transition. According to the measured R value, this maximum occurs at $t \simeq 5.5 \mu\text{s}$. Therefore, as previously assumed, saturation is reached within the $10 \mu\text{s}$ pulse duration even for the weak transition.

B. Photon echo

In this section, two-pulse photon echoes are achieved separately on each leg of the Λ . Application of a magnetic field splits the electronic levels, and repeated excitation achieves optical pumping between the two ground sub-levels. Therefore the echo is present as long as the temperature is high enough so that relaxation compensates for optical pumping.

Fig. 12 shows a two-pulse photon echo sequence in Tm:YAG under 0.3 T magnetic field, with a 50 s^{-1} repetition rate. The two pulses are gaussian and have equal

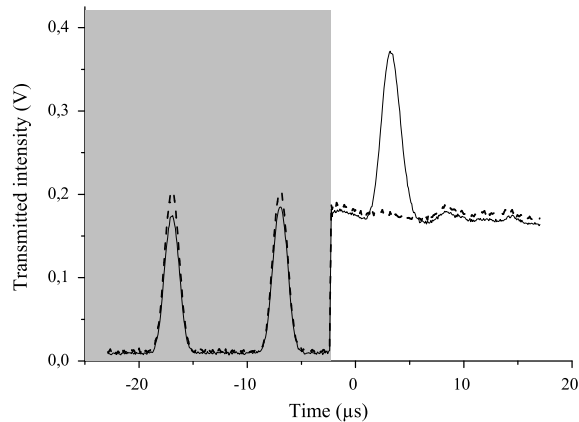


FIG. 12: Photon echo in Tm^{3+} : YAG under magnetic field with two gaussian pulses at $T = 2.6$ K (solid line) and $T = 1.9$ K (dashed line). The detection channel is gated by an acousto-optic modulator (AO 3 in Fig. 5) which attenuates the excitation pulses (grey area). This AOM opens a few μs after the second pulse to let the photon echo through. The echo disappears when optical pumping dominates thermalization.

intensity. At $T = 2.6$ K, thermalization still dominates the optical pumping caused by repeated excitation. In each two-pulse sequence, the first pulse partly bleaches the optical transition, so the second pulse is less absorbed than the first one. As the sample is cooled down, optical pumping becomes dominant. At $T = 1.9$ K, the resonant level is totally empty and the photon echo signal disappears. The excitation pulses propagate through a transparent medium where there is no bleaching process, which is why their transmitted intensities are equal.

We need to perform the same repumping process as described in Sec. VA in order to recover a signal and ascribe it to a weak or strong transition. When the repumping frequency is tuned to $\nu_0 \pm (\Delta_g - \Delta_e)$, ions in system (i) or (iii) in Fig. 10 are repumped and the photon echo is emitted along the strong transition at frequency ν_0 . When the repumping frequency is tuned to $\nu_0 \pm (\Delta_g + \Delta_e)$, the photon echo is emitted along the weak transition at frequency ν_0 in ions in system (ii) or (iv). To make sure that the detected signal is imputable to the weak transition, we slightly detune the repumping beam: the echo intensity goes down, which proves that the off-resonant repumping is less efficient and that the signal does not come from a residual signal emitted along a strong transition.

The photon echo amplitude can be expressed as a product of the transition dipole moment and a function of the Rabi frequency. This applies to both transitions, either strong or weak. Since the Rabi frequency is proportional to the transition dipole moment and to the applied field, the photon echo intensity along the strong transi-

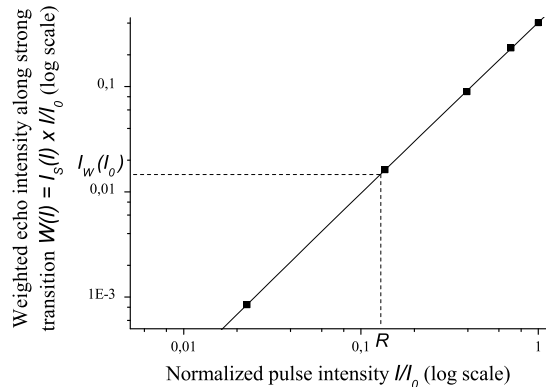


FIG. 13: Weighted echo intensity on the strong transition for different excitation pulse intensities (squares). These values are interpolated with a straight line (solid line) in order to solve Eq. 17. A graphical solution is given by the intersection point of $W(\mathcal{I}) = \mathcal{I}_s(\mathcal{I}) \times \mathcal{I}/\mathcal{I}_0$ and $W(\mathcal{I}) = \mathcal{I}_w(\mathcal{I}_0)$. The value is directly read out as $R = \mathcal{I}/\mathcal{I}_0$ at the intersection.

tion reads as:

$$\mathcal{I}_s(\mathcal{I}) = \mu_s^2 g(\mu_s^2 \mathcal{I}) \quad (14)$$

where \mathcal{I} represents the laser intensity and where the shape of function g need not be detailed any further.

Conversely, when the weak transition is excited with the same intensity \mathcal{I} , the photon echo intensity reads as

$$\mathcal{I}_w(\mathcal{I}) = \mu_w^2 g(\mu_w^2 \mathcal{I}) = R \mu_s^2 g(\mu_s^2 R\mathcal{I}) = R \mathcal{I}_s(R\mathcal{I}) \quad (15)$$

where R is the branching ratio.

The photon echo intensity \mathcal{I}_s on the strong transition is measured for different excitation intensities. A weighted echo intensity is defined as:

$$W(\mathcal{I}) = \mathcal{I}_s(\mathcal{I}) \times \mathcal{I}/\mathcal{I}_0 \quad (16)$$

This function is interpolated with a polynomial function as shown in Fig. 13. If we measure \mathcal{I}_w on the weak transition for a given intensity \mathcal{I}_0 , we are able to derive the branching ratio value by solving the following equation:

$$\mathcal{I}_w(\mathcal{I}_0) = R \mathcal{I}_s(R\mathcal{I}_0) \quad (17)$$

As shown in Fig. 13 and according to Eqs. 16 and 17, the graphical solution of this equation is given by the intersection point of $W(\mathcal{I}) = \mathcal{I}_s(\mathcal{I}) \times \mathcal{I}/\mathcal{I}_0$ and $W(\mathcal{I}) = \mathcal{I}_w(\mathcal{I}_0)$. The x -coordinate of this intersection point is the branching ratio R :

$$R = 0.130 \pm 0.015. \quad (18)$$

This is consistent too with the expectations derived from gyromagnetic factor measurements²³.

C. Discussion

With optical nutation and photon echo experiments we measured two branching ratio values that are in agreement with one another.

As far as theoretical gyromagnetic tensors are concerned, the (x, y) anisotropy is much larger in the ground state than in the excited state²⁴. This difference, known as *anisotropy disparity*, is at the origin of the high value for the maximum theoretical branching ratio $R_{\max} = 0.24$. The experimental value of anisotropy disparity appeared to be smaller than predicted by theory²³. As a result, a branching ratio value close to its lower boundary 0.13 was expected. The direct measurements presented in this paper confirm this result.

These measurements have been achieved for the magnetic field orientation ($\Theta = 49.4 \pm 0.2^\circ$) given by de Seze *et al.*²³. We did not study the dependence of R as a function of Θ . However, the branching ratio is almost constant over a 2° wide interval²⁴. Therefore, even with a 0.5° mechanical precision on the angle, one can reasonably consider that the measured branching ratio is close to its maximum.

Finally, in the experiments presented in Sec. V A, the nutation signal along the strong transition goes through its first maximum at $t = 2 \mu\text{s}$. This means that a π -pulse along the strong transition would take $1.2 \mu\text{s}$. According to the present branching ratio measurements, a π -pulse along the weak transition would then take $1.2/\sqrt{R} = 3.4 \mu\text{s}$. Therefore, we are able to excite each leg of the Λ system with a π -pulse, which is a capital asset in the perspective of coherent processes dynamics.

VI. CONCLUSION

We directly measure the transition probability ratio along the two legs of the Λ through coherent processes along with frequency selective optical pumping. This is performed in the optimum magnetic field orientation derived from a previous experiment²³. The direct measurement of the branching ratio is consistent with the value derived from the gyromagnetic tensor components and confirms that a Λ -system can operate efficiently in Tm:YAG. This way we have cross-checked and supported the theoretical description, complementing prior experimental data²³ with a new set of data different in nature. In addition, this provides us with the branching ratio value we have to know in order to efficiently build and control nuclear magnetic superposition states with optical excitation.

Side investigation on the sublevel lifetime leads to unexpected results. Indeed, broadly spaced sublevels appear to be more stable than closely spaced ones, in contradiction with previously reported experiments²⁶. This has to be clarified. Still, the measured lifetime is consistent with long-time coherent manipulation of spin states. The demonstrated existence of the Λ system promises interesting spin state properties in either ground or excited level. Next step will deal with the investigation of these coherent spin features.

-
- ¹ B. Julsgaard, A. Kozhekin and E. S. Polzik, *Nature (London)* **413**, 400 (2001).
- ² A. Kuzmich, W. P. Bowen, A. D. Boozer, A. Boca, C. W. Chou, L.-M. Duan and H. J. Kimble, *Nature (London)* **423**, 731 (2003).
- ³ T. Chanelière, D. N. Matsukevich, S. D. Jenkins, S.-Y. Lan, T. A. B. Kennedy and A. Kuzmich, *Nature (London)* **438**, 833 (2005).
- ⁴ E. Fraval, M. J. Sellars and J. J. Longdell, *Phys. Rev. Lett.* **92**, 077601 (2004).
- ⁵ A. V. Turukhin, V. S. Sudarshanam, M. S. Shahriar, J. A. Musser, B. S. Ham and P. R. Hemmer, *Phys. Rev. Lett.* **88**, 023602 (2002).
- ⁶ J. J. Longdell, E. Fraval, M. J. Sellars and N. B. Manson, *Phys. Rev. Lett.* **95**, 063601 (2005).
- ⁷ R. M. Macfarlane, *J. Lumin.* **100**, 1 (2002).
- ⁸ J. Mlynek, N. C. Wong, R. G. DeVoe, E. S. Kintzer and R. G. Brewer, *Phys. Rev. Lett.* **50**, 993 (1983).
- ⁹ L. E. Erickson, *Phys. Rev. B* **39**, 6342 (1989).
- ¹⁰ J. J. Longdell, M. J. Sellars and N. B. Manson, *Phys. Rev. B* **66**, 035101 (2002).
- ¹¹ R. Klieber, A. Michalowski, R. Neuhaus and D. Suter, *Phys. Rev. B* **67**, 184103 (2003).
- ¹² W. R. Babbitt, A. Lezama and T. W. Mossberg, *Phys. Rev. B* **39**, 1987 (1989).
- ¹³ S. Kröll, E. Y. Xu, M. K. Kim, M. Mitsunaga and R. Kachru, *Phys. Rev. B* **41**, 11568 (1990).
- ¹⁴ R. W. Equall, Y. Sun, R. L. Cone and R. M. Macfarlane, *Phys. Rev. Lett.* **72**, 2179 (1994).
- ¹⁵ K. D. Merkel and W. R. Babbitt, *Opt. Lett.* **23**, 528 (1998).
- ¹⁶ H. Lin, T. Wang and T. W. Mossberg, *Opt. Lett.* **20**, 1658 (1995).
- ¹⁷ V. Lavielle, I. Lorgeré, J.-L. Le Gouët, S. Tonda and D. Dolfi, *Opt. Lett.* **28**, 384 (2003).
- ¹⁸ G. Gorju, V. Crozatier, I. Lorgeré, J.-L. Le Gouët and F. Bretenaker, *IEEE Photon. Tech. Lett.* **17**, 2385 (2005).
- ¹⁹ B. P. Scott, F. Zhao, R. S. F. Chang and N. Djeu, *Opt. Lett.* **18**, 113 (1993).
- ²⁰ P. J. M. Suni and S. W. Henderson, *Opt. Lett.* **16**, 817 (1991).
- ²¹ V. Crozatier, F. de Seze, L. Haals, F. Bretenaker, I. Lorgeré and J.-L. Le Gouët, *Opt. Comm.* **241**, 203 (2004).
- ²² A. Abragam and B. Bleaney, *Electronic Paramagnetic Resonance of Transition Ions* (Clarendon Press, Oxford, 1970), chap. 15.
- ²³ F. de Seze, A. Louchet, V. Crozatier, I. Lorgeré, F. Bretenaker, J.-L. Le Gouët, O. Guillot-Noël and Ph. Goldner, *Phys. Rev. B* **73**, 085112 (2006).

- ²⁴ O. Guillot-Noël, Ph. Goldner, E. Antic-Fidancev and J.-L. Le Gouët, Phys. Rev. B **71**, 174409 (2005).
- ²⁵ V. H. Schmidt and E. D. Jones, Phys. Rev. B **1**, 1978 (1970).
- ²⁶ N. Ohlsson, M. Nilsson, S. Kröll and R. Krishna Mohan, Opt. Lett. **28**, 450 (2003).
- ²⁷ Y. Sun, G. M. Wang, R. L. Cone, R. W. Equall and M. J. M. Leask, Phys. Rev. B **62**, 15443 (2000).
- ²⁸ E. L. Hahn, Phys. Rev. **80**, 580 (1950).